Sky Noise Limited Snapshot Imaging in the Presence of RFI with LOFAR's Initial Test Station

Stefan J. Wijnholds, Jaap D. Bregman, Albert-Jan Boonstra

January 19, 2007

Abstract

The Initial Test Station is the first full scale prototype of a LOFAR station. It operates in the 10-40 MHz range and consists of 60 sky noise limited dipoles arranged in a five-armed spiral structure offering an instantaneous synthesized aperture of almost 200 m diameter. We will present all sky snapshot images demonstrating sky-noise limited imaging capability in the presence of a strong RFI source that exceeds the all sky power by 27 dB. This result is obtained with a two stage self-calibration procedure. First the RFI source near the horizon is used as calibrator and then subtracted, after which Cas A shows up at a level that is a factor 2000 lower and then dominates the picture with its side lobes. A second self calibration on Cas A then reveals the same extended galactic emission as found in a RFI free adjacent spectral channel. This demonstrates that a single 10 kHz channel of a 6.7 s snapshot of a single LOFAR station already provides a dynamic range of over 10^4.

1 Introduction

The Low Frequency Array (LOFAR) is a radio telescope currently being designed and planned. Its targeted observational frequency window lies in the range 10-250 MHz. LOFAR will consist of a number of stations spread over an area of 350 km diameter. Each station consists of order 100 receiving elements which operate together as a phased array. The initial test station (ITS) is the first full scale prototype of a LOFAR station and became operational in December 2003. In this paper we will demonstrate that this system may be used to do sky noise limited snapshot imaging in the presence of RFI. This is an important milestone towards sub-milliJansky imaging at these low frequencies. As pointed out by Boonstra et al. [1][2] RFI signals need only be reduced to the noise level of an individual snapshot image. Further integration to improve the SNR implies rotation of the sky relative to a hemispheric image. This has the consequence that after derotation the sky sources improve in SNR while point sources appearing at various fixed locations, like RFI, decrease in SNR and will become invisible.
In the next section we will provide a short description of ITS before proceeding with a mathematical description of the processing done to obtain the image and to perform the calibration. Once the processing is clearly described we will demonstrate the sky noise limited performance by presenting a plot of the differences between two neighboring channels after calibration on a RFI source in a nearby channel. Thereafter we will show that Cas A appears when the RFI source is self calibrated and removed by standard CLEAN techniques. Finally we will show that after removal of the RFI source, the calibration result can be improved further by another calibration on Cas A.

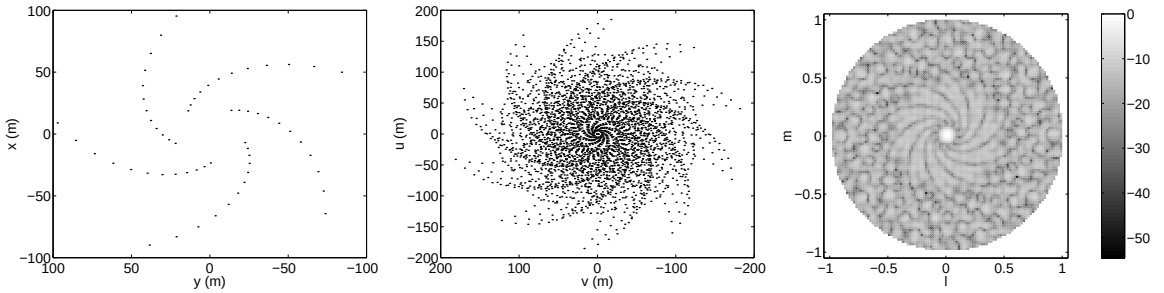

Figure 1: The left hand plot shows the configuration of the ITS antennas. Positive x is pointing north, positive y is pointing west. The middle plot shows the (u, v)-coverage for a single snapshot. The baselines are depicted in meters instead of wavelengths for convenience since ITS covers a factor 4 in frequency (10-40 MHz). Finally, the beam pattern of ITS at 30 MHz is shown in the right hand panel. The sensitivity is depicted in dB, 0 dB being the sensitivity of the main lobe pointed towards the zenith.

2 ITS system overview

ITS consists of 60 sky noise limited inverse V-shaped dipoles with East-West orientation. The dipoles are arranged in a five armed spiral configuration as shown in figure 1. The instantaneous or snapshot (u, v)-coverage and the beam pattern or PSF are also displayed in this figure.

Each antenna samples the same single polarization and is connected to a receiver unit where the signal is filtered by a 10-40 MHz bandpass filter and digitized by a 12 bit A/D converter before it is transmitted over a high speed optical link to a twin input module (TIM) board. The TIM board is a data acquisition card having two high speed optical link receivers, 2 GB of RAM buffer and a PCI interface for read-out and control, which was developed at ASTRON.

The on-site data acquisition and processing system consists of 16 standard PC's (2.4 GHz Intel Xeon, 1 GB RAM, Linux 2.4.20) for data acquisition and initial processing, 1 industrial PC for central processing and data storage (dual 2.0 GHz Intel Xeon, 512 MB RAM, Linux 2.4.20) and 1 router (2.4 GHz Intel Xeon, 1 GB RAM, Linux 2.4.21). The PC's are interconnected by a 100 Mbit control network and a 1 Gbit data network.

Each data acquisition PC is equipped with two TIM boards, giving the full system a capacity of 64 input channels. On these machines the raw data from the individual antennas $x_i[n]$, where the subscript i denotes the antenna number, can be acquired from the TIM boards. These signals can be sent to the central processing and storage machine directly, but they also offer some initial processing options, such as statistics computation and Fourier transform. The central processing and storage machine can either store the incoming data or do some additional processing, such as beam forming or correlation.

3 Data reduction theory

For our observations we used the data acquisition PC's to do a fast Fourier transform on the acquired time series $x_i[n]$. For this operation the data was split up in non-overlapping blocks of N_{FFT} samples each forming a single snapshot. A Hanning taper $w_{han}[n] = \frac{1}{2}(1 -$

$\cos(2\pi n/N_{FFT})$) was applied to each snapshot (with index m) before doing the actual Fourier transform to obtain

$$y_{i,m}[k] = \sum_{n=0}^{N_{FFT}-1} w_{han}[n] x_i[n + mN_{FFT}] e^{-2\pi jnk/N_{FFT}}. \quad (1)$$

Since the rest of the discussion focuses on operations on a single frequency channel, we will drop the explicit statement of the dependence on k, i.e. $y_{i,m} = y_{i,m}[k]$. On the central processing and storage machine, first a full correlation matrix for every individual snapshot

$$\mathbf{R}_m = \mathbf{y}_m \mathbf{y}_m^H \quad (2)$$

is calculated. In this equation $\mathbf{y}_m = [y_{1,m}, y_{2,m}, ..., y_{p,m}]^T$ where the number of used elements is p and the superscript H denotes the Hermitian transpose. Before storage this result is integrated over M snapshots to arrive at the integrated array correlation matrix (ACM)

$$\mathbf{R} = \sum_{m=0}^{M-1} \mathbf{R}_m. \quad (3)$$

Beam steering in phased array telescopes can be done by applying complex weights w_i to the individual elements such that signals from the selected direction are added coherently. The voltage output of the beam former can thus be described as

$$A_m = \mathbf{w}^T \mathbf{y}_m \quad (4)$$

where $\mathbf{w} = [w_1, w_2, ..., w_p]^T$. The power output of the beam former after integration over M snapshots will be

$$|A|^2 = \sum_{m=0}^{M-1} A_m \overline{A_m}, \quad (5)$$

where $\overline{A_m}$ denotes the complex conjugate of A_m. This result can also be obtained using the ACM, since

$$\begin{aligned}
\overline{\mathbf{w}}^H \mathbf{R} \overline{\mathbf{w}} &= \mathbf{w}^T \left(\sum_{m=0}^{M-1} \mathbf{y}_m \mathbf{y}_m^H \right) \overline{\mathbf{w}} & (6)\\
&= \sum_{m=0}^{M-1} \left(\mathbf{w}^T \mathbf{y}_m \right) \left(\mathbf{y}_m^H \overline{\mathbf{w}} \right) & (7)\\
&= \sum_{m=0}^{M-1} A_m \overline{A_m} & (8)\\
&= |A|^2 & (9)
\end{aligned}$$

The theory presented up to this point assumes a perfectly calibrated array where all elements have intrinsic gain 1, so the output of the beam former is completely determined by the input signal and the beam forming weights. In practice element i will have intrinsic gain g_i and receiver noise power σ_i^2. These properties can be summarized in vector $\mathbf{g} = [g_1, g_2, ..., g_p]^T$

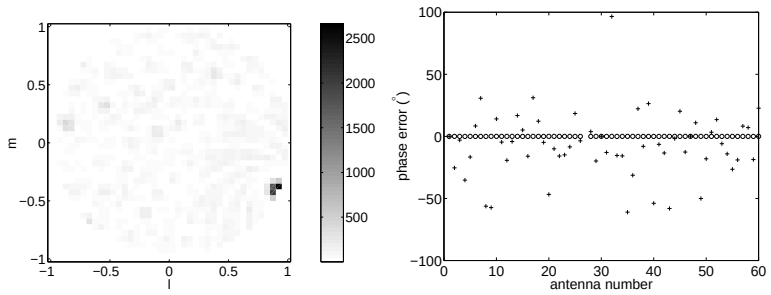

Figure 2: The full sky image shown in the left panel is based on a full correlation matrix for a 9.77 kHz wide frequency channel around 18.916 MHz from a 6.7 s observation on February 26, 2004 at 3:50 AM. The image is completely dominated by the RFI source on the south-eastern horizon. The image values are the direct result from equation 6 after normalizing $\mathbf{R}$ such that all its diagonal elements are equal to 1. The right hand plot shows the phase errors of the individual signal paths before (+) and after (o) calibration on the RFI source. The standard deviation before calibration is 26.5°, after calibration it is only 0.0011°.

and vector $\boldsymbol{\sigma}^2 = [\sigma_1^2, \sigma_2^2, ..., \sigma_p^2]^T$ respectively. If the ACM as would be measured at an ideal noiseless array is denoted by R_0, then the measured ACM will be

$$\mathbf{R} = \mathbf{g}\mathbf{g}^H \odot \mathbf{R}_0 + \mathrm{diag}(\boldsymbol{\sigma}^2) \tag{10}$$

where $\odot$ denotes element-wise multiplication of two matrices and $\mathrm{diag}(\boldsymbol{\sigma}^2)$ is the diagonal noise matrix. The elements of $\mathbf{R}$ represent the sky brightness spatially integrated by the antenna elements.
If the system is sky noise limited, the receiver will contribute less to the autocorrelation power than the sky. Therefore the second term in equation (10) can be neglected. Thus

$$\mathbf{g}\mathbf{g}^H = \mathrm{R} \oslash \mathrm{R}_0 \tag{11}$$

where $\oslash$ denotes element-wise division of two matrices. The gain vector $\mathbf{g}$ is now the Eigen vector corresponding to the largest Eigen value of $\mathbf{g}\mathbf{g}^H$.

4 Sky noise limited snapshot imaging

In this section we will demonstrate the near sky noise limited behavior of the ITS after calibration. The starting point will be a 6.7 s observation done on February 26, 2004 at 3:50 AM. A 8192 point FFT was used and integrated ACM's were computed based on the first 4096 Fourier coefficients providing ACM's for 9.77 kHz wide frequency channels covering the full range from 0 to 40 MHz.
As shown in the left panel of Fig. 2 the 9.77 kHz band around 18.916 MHz is completely dominated by an RFI source on the south-eastern horizon. This source was used as calibration source following the procedure outlined in the previous section. The right hand panel of Fig. 2 shows that this greatly reduces the phase errors in the individual signal paths (standard deviations before and after calibration are 26.5° and 0.0011° respectively). The errors after calibration are the combined result from neglecting the finite sample effect and ignoring the sky and system noise contributions.

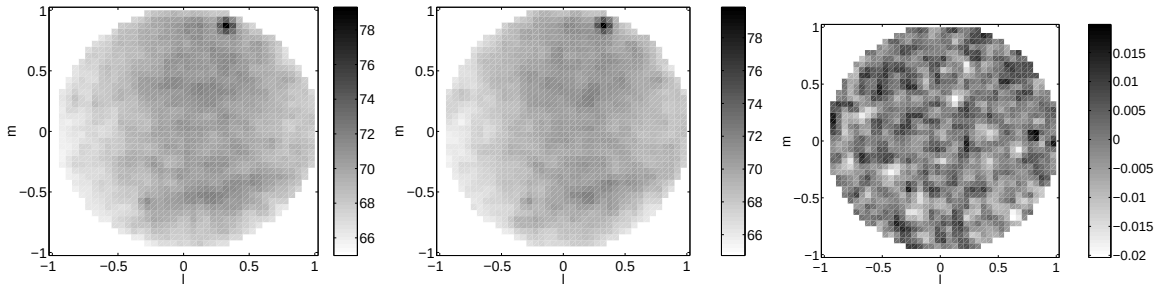

Figure 3: The left and middle panel show full sky images based on full correlation matrices for two 9.77 kHz frequency channels centered around 18.760 (left) and 18.779 MHz (middle) from the same 6.7 s observation as mentioned in the caption of Fig. 2. The image values are the direct result from equation 6 after normalizing $\mathbf{R}$ such that all its diagonal elements are equal to 1. Both images show the sky background with the north galactic spur on the southern hemisphere and Cas A near the northern horizon. The right panel shows the differences between the two maps. The image values are expressed as fractions of the sky background levels in the left and middle plots. The standard deviation of the image values is 0.0057.

The phase errors before calibration are partly frequency dependent due to path length differences in the analog circuitry and partly frequency independent due to slightly different responses of the analog filters. Since there is only a gradual change in the phase over frequency, we can safely apply the calibration data at 18.916 MHz to two neighboring RFI free frequency channels centered around 18.760 and 18.779 MHz from the same observation. The resulting images are shown in the left and middle panel of Fig. 3.
The right panel of the same figure shows the differences between these two sky images. The differences are expressed as fractions of the sky background level in these sky maps. The standard deviation of the image values of 0.0057. If the system is sky noise limited, one would expect the noise in the individual sky maps to be $\frac{T_{sky}}{\sqrt{B\tau}}$ where T_{sky}, B and τ denote the sky noise temperature, the bandwidth and the integration time. Based on the observational parameter, one would thus expect the noise to be a fraction 0.0039 of the sky noise. This should be multiplied by $\sqrt{2}$ for the difference image giving an expected value of 0.0055. From the agreement between the measured (0.0057) and the expected (0.0055) values we can conclude that the system has sky noise limited performance.

5 Spatial RFI removal using CLEAN

The CLEAN algorithm removes a point source with power σ^2_{src} in the visibility domain. In terms of spatial filtering this is called subtraction filtering [1] and can be described as

$$\mathbf{R}_{-} = \mathbf{R} - \sigma^2_{src}\mathbf{a}\mathbf{a}^H \tag{12}$$

where $\mathbf{a} = [a_1, a_2, ..., a_p]^T$ describes the ideal array response to a point source of unit power at position (l_{src}, m_{src}).
When the source in the left panel of Fig. 2 is subtracted from the image in the image domain before calibration, the image in the left panel of Fig. 4 is obtained. The values are expressed as percentage of the peak value in the original image. This shows that the differences between

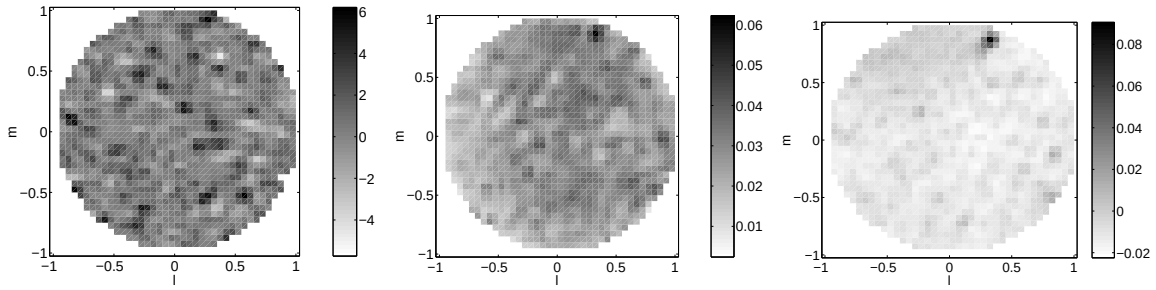

Figure 4: The left panel shows a full sky image of the RFI invested channel of Fig. 2 after subtracting the RFI source in the image domain without calibration. The image values are represented as percentage of the peak value in the original image. This shows differences between the expected and the actual beam pattern as large as 5% of the maximum. The middle panel shows the result after subtraction of the RFI source in the visibility domain after calibration on the same scale. In this image Cas A becomes visible. The right panel shows a full sky image after another calibration on Cas A, an approach called peeling.

the expected beam pattern and the actual beam pattern are as large as 5% of the maximum.

When subtraction is done in the visibility domain using the procedure outlined above but deriving the necessary parameters (σ^2_{src} and (l_{src}, m_{src})) from the image after calibration, the sky map in the center panel of Fig. 4 is obtained. Although the power estimate was not perfect as can be seen from the fact that there is an "absorption" feature at the location of the RFI source, the image clearly shows Cas A on the northern horizon. This plot also shows that the ITS approximates the behavior of an ideal array within 0.05% otherwise we would not be able to see significant features at this level.

Finally an attempt was made to refine the calibration parameters by recalibrating the array correlation matrix obtained after subtraction of the RFI source using Cas A. This approach, which is called peeling [3], resulted in the sky map shown in the right panel of Fig. 4. This image clearly shows extended emission along the northern horizon which can be identified with the galactic plane. This shows that even with a single LOFAR station significant features of 0.01% of the strongest source in the field can be detected indicating a usable dynamic range of over 10^4. It also shows blobs of similar power in other parts of the sky which can not be identified with astronomical sources. We therefore conclude that these are artefacts due to imperfect subtraction of the RFI source.

This image also shows a shortcoming of the point source calibration approach in that it assumes an isotropic element beam pattern, which does not hold for the inverse V-shaped dipoles of the ITS. This becomes apparent when comparing sky noise intensity distribution in the image in the middle panel of Fig. 4 with that in the right panel of the same figure. In the middle panel it clearly decreases toward the western horizon due to the reduced sensitivity of the individual elements at low elevation. The calibration routine assumes that a single point source is the only structure on the whole sky and will thus flatten out any other structure that may be present. This causes the sky noise to look completely homogeneous in the right panel.

6 Conclusions

Based on a 6.7 s observation in a 9.77 kHz band it was shown that a single LOFAR station closely resembles the behavior of a sky noise limited system in a single snapshot. This has been achieved by a simple spectral Hanning taper for the whole 10-40 MHz band sampled by a 12 bit ADC.
We have also demonstrated that astronomical observations can be done in the presence of RFI using standard astronomical approaches. To this end a RFI invested image from a 6.7 s observation in a 9.77 kHz band around 18.916 MHz was taken. After selfcal on the RFI source and using CLEAN to remove it from the image Cas A and some emission from the galactic plane became visible indicating a dynamic range of over 10^4.
A suitable point source calibration approach for sky noise limited systems was presented in this paper. The results obtained in the paper implicitly show that this calibration technique attains the required level of accuracy; strong RFI signals can be used for initial complex gain calibration to a level of $3 \cdot 10^{-6}$, limited by the noise fluctuations in the system. For other positions on the sky we obtain a dynamic range of only 10^4, which is however enough for the strongest sky source.

References

[1] Boonstra, A.J., Tol, S. van der *Spatial filtering of interfering signals at the initial LOFAR phased array test station, to be submitted to:* Radio Science, Special issue on interference mitigation in radio astronomy

[2] Veen, A.J. van der, Leshem, A., Boonstra A.J. *Signal Processing for Radio Astronomical Arrays*, SAM workshop, Barcelona (Spain), July 18-21, 2004

[3] Noordam, J.E. *LOFAR calibration challenges*, SPIE conference on astronomical telescopes and instrumentation, Glasgow (UK), June 21-25, 2004